

Contents list available at CBIORE journal website

Remarkable Energy Development

Journal homepage: https://ijred.cbiore.id



Research Article

Synthesis of rubber seed shell-derived porous activated carbons for promising supercapacitor application

Heri Rustamaji^{a*} , Tirto Prakoso^b , Hary Devianto^b, Pramujo Widiatmoko^b , Pramahadi Febriyanto^{b,c} , Simparmin br Ginting , Darmansyah Darmansyah o

Abstract. This work investigates synthesizing activated carbon obtained from rubber seed shells utilizing several activating agents (KOH, CaCl₂, and ZnCl₂) for supercapacitor applications. Activated carbon was produced from a rubber seed shell using hydrothermal carbonization at 275 °C for 60 minutes and a 120-minute activation treatment at 800 °C. Various activating agents pronounced impacted the pore architecture, surface area, crystallinity, and level of graphitization, which collectively determined the electrochemical characteristics of the resulting materials. Incorporating activation agents enhances the specific surface area and influences the extent of graphitization of activated carbon. The specific surface area of activated carbon products ranges from 367 to 735.2 m² g⁻¹. Further investigation through electrochemical analysis, conducted with a carefully engineered two-electrode system, demonstrated a peak electrode capacitance value of 246 F g⁻¹ at 50 mA g⁻¹ for an ACZn-based supercapacitor. Supercapacitor cells' energy and power densities reached significant levels, measuring 5.47 Wh kg⁻¹ and 246 W kg⁻¹, respectively. The RSS-derived activated carbon-based supercapacitor exhibited remarkable longevity in a 5000-cycle test, with consistent capacitance retention and coulombic efficiency of 100.11% and 100%, respectively. This work presents a sustainable pathway for producing activated carbon electrodes, contributing to the global circular economy and demonstrating considerable industrial potential.

Keywords: rubber seed shell, hydrothermal carbonization, pyrolysis, supercapacitor, electrochemical performance.



@ The author(s). Published by CORE. This is an open-access article under the CC BY-SA license. (http://creativecommons.org/licenses/by-sa/4.0/). Received: 19th Nov 2024; Revised: 5th January 2025; Accepted: 26th January 2025; Available online: 10th February 2025

Introduction 1.

Renewable energy is currently at the forefront of research trends due to the world's extreme energy needs and ecological considerations. Efficient energy storage systems are crucial to optimize the utilization of renewable energy sources. Presently available energy storage technologies, including lithium-ion batteries (LIBs), are confronted with issues related to their modest power density and sluggish charging and discharging pace (Simon & Gogotsi, 2020). As a result, developing a unique energy storage technology is critical and continues to be a significant issue. Supercapacitors (SCs) are widely favored for energy storage because they offer rapid energy discharge, high power density, and exceptional cycling durability as opposed to batteries. Supercapacitors are also recognized for their effective performance across a broad temperature range. However, their primary drawback is their relatively low energy density (Gunasekaran et al., 2021).

The performance characteristics of all three supercapacitor variants—double-layer capacitors (DLCs), pseudocapacitors, and hybrid capacitors—are intricately governed by a confluence of factors, including the specific surface area, pore morphology, electronic conductivity, and the exterior chemical of material's electrode. These attributes collectively dictate the charge storage mechanisms, ion accessibility, and electrochemical behavior, thereby influencing the efficiency and energy density of the devices (Zhao & Burke, 2021).

Electrode materials with extensive surface areas and optimal pore structures can store charge, while excellent electrical conductivity enhances the movement of charges across the electrolyte and electrode contact. Faradaic redox reactions are enabled by heteroatoms and surface functional groups and thus increase capacitance (Abdul et al., 2021; Veeman et al., 2021). The primary goal is to create electrode materials with the best matching ability to store and transport charges. Carbon material-based supercapacitor electrodes have recently been reported as potential candidates because of their high surface area, porosity, electrical conductivity, and surface functions. This characteristic is because a lot of effort has been put into the development of supercapacitor electrodes based on activated carbons from biomass since these can be both economical and sustainable in the long run (Dujearic-Stephane et al., 2021; Lawtae & Tangsathitkulchai, 2021).

With a diverse range of rubber agricultural by-products, seed shells are potentially utilized as precursors for synthesizing activated carbon (AC). Rubber seed shells (RSS) comprise 72%

^aDepartment of Chemical Engineering, Lampung University, Indonesia

^bDepartment of Chemical Engineering, Bandung Institute of Technology, Indonesia

^cDepartment of Chemical Engineering, Sumatera Institute of Technology, Indonesia

Corresponding author Email: heri.rustamaji@eng.unila.ac.id (Rustamaji)

cellulose, 25% hemicellulose, and 3.0% lignin (Kanjana *et al.*, 2021). Due to their low cost and year-round availability, biomass resources are excellent precursors for activated carbon production and other biomass processing applications. The preliminary stage in the biomass valorization chain is the drying process. This process is a critical step to mitigate storage and transportation expenses and improve the efficiency of subsequent operations, including carbonization and pyrolysis. The mechanisms underlying drying encompass the diffusion of bound moisture alongside the material transport of free water at controlled temperatures. The moisture content must remain below 10% to ensure optimal processing conditions (Rustamaji *et al.*, 2023; Yu *et al.*, 2021).

This has been accompanied by an increased interest in biomass utilization on a global scale. The standard industrial practice of producing activated carbon (AC) is a direct-fired rotary dryer that uses a furnace to burn natural gas as fuel (Abdul *et al.*, 2021). The next crucial stage following the drying process is activation. Physical and chemical activation methods are mainly used to transform natural waste into activated carbon. Physical activation generally occurs by heating the AC precursor in a continuous stream of steam or gases (Abdel Maksoud *et al.*, 2021; Das & Verma, 2019).

Wood and plant-based materials undergo a process where they are chemically treated with substances, like zinc chloride and potassium hydroxide, under temperatures and pressures to activate them for purposes. This activation process creates pores in these materials while controlling their size distribution effectively. Moreover, these treated materials can also be used in a self-activation method where cations, from activating chemicals, get embedded into the material during a carbonization process involving water and heat (Abdel Maksoud et al., 2021). This phenomenon is when porous activated carbon products are formed due to physical activation at high temperatures. In addition, such substances are usually employed as electrolytes, which leads to the fact that the pore widths of the activated carbons are equal to the radii of the ions, which enhances charge storage and transfer (Cheng et al., 2020; Tagaya et al., 2020).

The present work focuses on preparing activated carbons from rubber seed shells (RSS) for supercapacitors using KOH, ZnCl₂, and CaCl₂ activation methods after hydrothermal carbonization (HTC) and pyrolysis activation. However, despite many attempts to prepare activated carbons from these feedstocks, no specific attention has been paid to rubber seed shells or the comparison of the three activating agents (KOH, ZnCl₂, and CaCl₂) through HTC regarding their application in supercapacitors (Han *et al.*, 2020; Mostazo-López *et al.*, 2019).

Furthermore, the current work is the first to optimize the two-step processing of rubber seed shells (RSS) for producing supercapacitors using three different activating agents. Hydrothermal carbonization (HTC) was performed at 275 degrees Celsius to carbonize rubber seed shells. Pyrolysis followed this process in a nitrogen environment at 800 degrees Celsius. Investigations were also conducted into the physicochemical features of the activated carbon system and the electrochemical properties of the activated carbon compounds when they were used as electrodes for supercapacitors.

2. Materials and Methods

2.1 Synthesis of activated carbon

The generation of activated carbons (ACs) from rubber seed shells (RSS) is investigated in this study. Several different

substances were used to investigate the activation agents. The activation agents that were used in the investigation include Calcium Chloride (CaCl₂, Merck, 99.5% wt), Zinc Chloride (ZnCl₂, Merck, 99.5% wt) and Potassium Hydroxide (KOH, Merck, 99.5% wt). Hydrogen chloride acid (HCl, Merck, 37% vol) was used to rinse the activated carbon products after they had been processed.

The compounds were procured from Merck in analytical grade and did not require additional treatment. Demineralized water provided uniformity throughout the experiment. The biomass was subjected to a thorough cleaning and drying procedure. The materials underwent size reduction by combining cutting and grinding methods, resulting in a consistent particle size of 250 micrometers. In hydrothermal carbonization, each biomass type was carefully mixed with a solution of activating chemicals, prepared at half biomass mass ratios. The resultant mixes were enclosed in a sealed stainless reactor and exposed to thermal processing at 275 °C for 1 hour (Rustamaji *et al.*, 2023).

After the hydrothermal treatment, the resultant hydrochars were thoroughly washed to remove any leftover potassium ions clinging to their surfaces. Thereafter, they were desiccated at a controlled temperature of 60 °C overnight. The third step involved physical activation, achieved by exposing the hydrochars to a temperature of 800 °C for 2 hours in a nitrogen stream environment, with an adjusted thermal rate of 10°C min-¹. The synthesized ACs were subjected to a 10% hydrochloric acid solution for one hour. This was succeeded by extensive rinsing with demineralized water to achieve a 5-6 pH. The products were dried overnight at 105°C, cooled, and placed in a desiccator for the next investigation (Rustamaji et al., 2022). To enable effective identification, the ACs were assigned based on a nomenclature scheme that incorporates the biomass source and the activating agent utilized, maintaining a biomass ratio of 1:2. Activated carbons produced with KOH, CaCl₂, ZnCl₂, or in their unmodified state are referred to as ACK, ACCa, ACZn, and ACO, respectively.

2.2 Physical characterization

The scanning electron microscopy coupled with energydispersive X-ray spectroscopy (SEM-EDS) method (Zeiss, MERLIN Compact-Oxford, Aztec ED) was utilized to investigate the morphological characteristics and atomic composition of the activated carbons that were brought into existence. To assess the surface functionality of a BRUKER Tensor 27, Fourier Transform Infrared Spectroscopy (FTIR) was employed, with the scan range extending from 4500 to 550 cm⁻¹. Raman spectroscopy (XploRA PLUS Raman, HORIBA) was performed using a 532 nm laser wavelength. At the same time, X-ray diffraction spectrometry (XRD, Bruker) employed Cu K-α radiation ($\lambda = 1.5406 \text{ Å}$) to analyze the crystalline structure of the materials. The surface characteristics of the porous carbon materials were assessed with a porosimetry analyzer (Quantachrom Instruments, USA), applying the Brunauer-Emmett-Teller (BET) and Barrett-Joyner-Halenda (BJH) methodologies.

2.3 Fabrication of supercapacitor and electrochemical characterization

Researchers developed an electrode utilizing activated carbon, enhanced with a 10% weight fraction of PVDF adhesive. The composite was dispersed in ethanol and subjected to ultrasonication employment for 25 minutes. The dried

composite was carefully pelletized to a total weight of 0.2 g under pressures ranging from 7 to 10 MPa. The technique produced a CR2302 size coin cell with a load of 2.3 mg cm⁻² and bicircular electrodes. The 6 M KOH solution approximately 3 ml was dripped onto the surface of the two electrodes until was absorbed into the electrode pores. Then, the two electrodes are separated with Whatman filter paper, which has also been dripped with electrolytes. After all the components of the coin cell are arranged, they are pressed using a crimping machine. The coin cell is placed in a cell holder with positive and negative poles and is ready to be tested (Rustamaji *et al.*, 2022).

To conduct a comprehensive investigation of the electrochemical properties, a Gamry ZRA galvanostat was utilized in conjunction with two electrode systems to measure the working and counter electrodes. Given this, the galvanostatic charge-discharge (GCD) experiments that were carried out for this investigation were carried out at current densities ranging from 30 to 100 milliamperes. The cyclic voltammetry (CV) measurements were performed with high accuracy, and the scan rate was varied from 4 to 12 millivolts per second. The electrochemical impedance spectroscopy (EIS) was done carefully over a frequency of 0.01–100,000 Hz. Furthermore, a full charge-discharge study of 5000 cycles was carried out to assess the system's lifespan. With the help of Equation (1), we could also determine the specific capacitance of the cell denoted by Ccell (Dujearic-Stephane *et al.*, 2021).

$$C_{cell} = \frac{I \, \Delta t}{m \, \Delta V} \tag{1}$$

$$C_{sp} = 4C_{cell} \tag{2}$$

For the capacitance of the cell, C_{cell} , the capacitance, C (F g $^{-1}$), the total load of the symmetrical electrode, m (g), and the current, I (A), of the cell, Equation 2 was used. Equations (3) and (4) were employed to determine energy and power per unit mass (E_{cell} in Wh kg $^{-1}$, P_{cell} in W kg $^{-1}$) from charge-discharge measurement, using equations (3) and (4) (Wu *et al.*, 2020).

$$E_{cell} = \frac{1}{2} \frac{C_{cell} \Delta V^2}{3.6} \tag{3}$$

$$P_{cell} = \frac{3600 \, E_{cell}}{\Delta t} \tag{4}$$

 $\Delta t \ \& \ \Delta V$ represent period (s) and voltage (V) during the charge release process.

3. Results and Discussion

3.1 Physical properties

The surface morphology of activated carbon that was created from RSS using various activation chemicals was studied through scanning electron microscopy, and the images obtained are displayed in Figure 1. The surface structures of any product are chaotic and uneven. The surface of AC0 synthesized without an activating agent exhibits some rounded properties and a less defined pore structure (Figure 1a). All AC samples exhibit well-developed porous structures upon the addition of activating agents. The surface of ACCa (Figure 1c) shows a porous nature with structural voids. In contrast, the surface of ACK (Figure 1b) displays a pore architecture characterized by interconnected pore clusters of the modified activated carbon. The influence of activating agents on morphological structure.

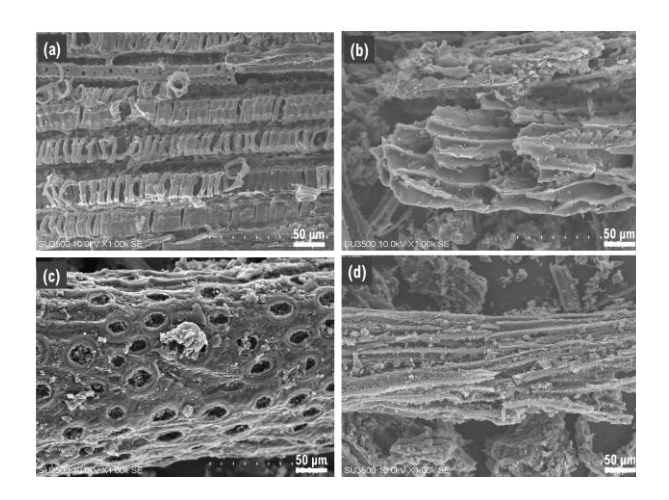
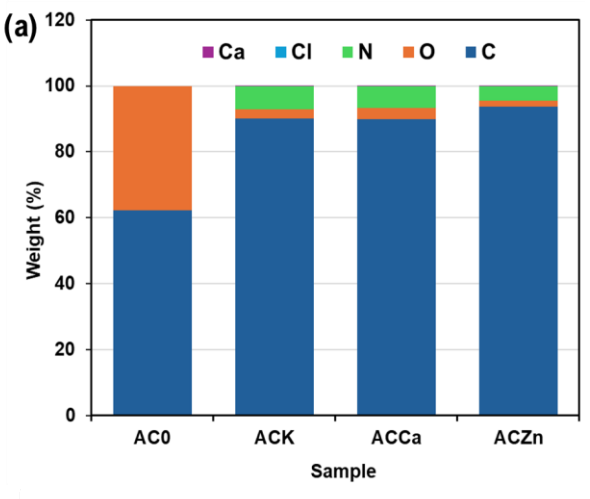


Fig. 1. Scanned electron microscopy of the (a) AC0, (b) ACK, (c) ACCa, and (d) ACZn.

The SEM micrographs indicate that the activating agents' efficacy in enhancing biomass porosity is ACZn > ACK > ACCa > AC0. The shape, especially the existence of cavities, is essential for energy storage, as these cavities facilitate the retention of electrolyte ions. The construction of a few uneven cavities on the material exterior is associated with the thermal



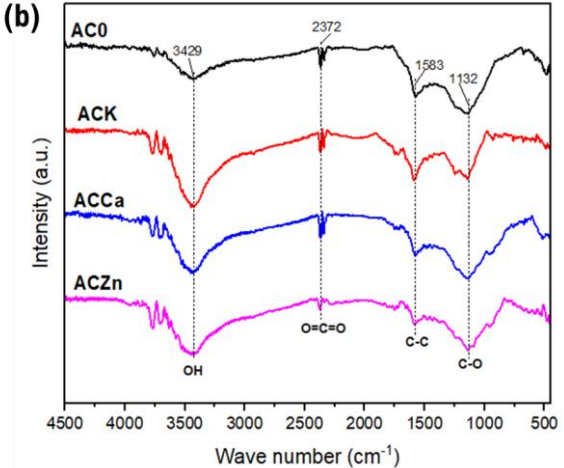


Fig. 2. (a) EDS examining the atomic composition and (b) IR spectrum of all synthesized activated carbon.

degradation of lignocellulosic materials, resulting in the evaporation of volatile chemicals and the development of new pores (Cheng *et al.*, 2020; Wang *et al.*, 2020).

Energy-dispersive X-ray spectroscopy (EDS) was utilized to examine a qualitative of the elemental fraction of the activated carbon (AC) surface. The EDS outcome indicated that the AC samples primarily comprised carbon and oxygen. At the same time, trace elements constituted less than 5%, as demonstrated in Figure 2a. Figure 2a indicates that incorporating an activating agent elevates carbon concentration while diminishing oxygen levels. Introducing an activating agent promotes the removal of hydrogen and oxygen from the precursor material, leading to a minimal loss of volatile substances and tars; hence, a comparatively high reaction yield is achieved.

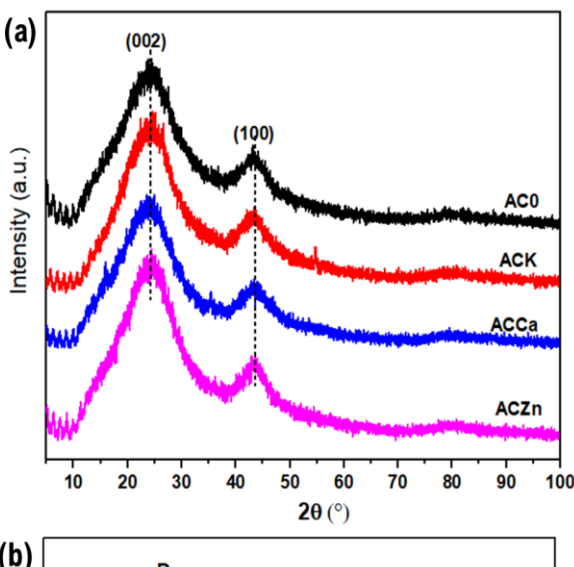
The functional groups of the produced activated carbons were examined utilizing the FTIR technique. Figure 2b illustrates that the FITR spectra of activated carbons are analogous, demonstrating various functional groups typically present in activated carbon (Shabik *et al.*, 2020). We focus on heteroatom-containing functional groups, recognized for their impact on the electrostatic characteristics of the produced porous carbon. The vibrational frequencies for the AC framework are as follows: OH extending (about 3429 cm⁻¹), CH extending (approximately 2920 cm⁻¹), C=O stretching (approximately 2372 cm⁻¹), CH extending (approximately 2331 cm⁻¹), C-C extending (approximately 1582 cm⁻¹). C-O extending (approximately 1132 cm⁻¹).

The activated carbon surface may exhibit diverse functional groups, encompassing aromatic rings, primary alcohols, phenolic compounds, and carboxylic acids, each contributing to its chemical reactivity and interaction properties. Electrode materials loaded with heteroatoms enhance charge transfer and capacitance in aqueous electrolytes, rendering them optimal for supercapacitor applications, although there is none in this instance (Gopalakrishnan & Badhulika, 2020; Lin et al., 2021).

Figure 3a illustrates the XRD studies of pure and porous carbon products utilizing different activating agents. The XRD appearances in every example show a prominent peak (002) at $2\theta = 26^{\circ}$ and a subtle band (100) at $2\theta = 43^{\circ}$. The diffraction band corresponds to hexagonal carbon, as per JCPDS standard no. 41-1487 (Han *et al.*, 2020). The prominent peak at (002) indicates amorphous carbon post-activation, whereas the decline at 100 signifies graphitic carbon. As an additional point of interest, the crystallinity percentages of AC0, ACK, ACCa, and ACZn products were 19.3%, 21.8%, 16.2%, and 21.7%. A higher proportion of crystallinity is correlated with activating substances, as this figure highlights the correlation.

The activated carbon's chemical characteristics underwent a comprehensive analysis through Raman spectroscopy, with the resulting spectra illustrated in Figure 3b. The notable peaks identified at 1330 cm⁻¹ and 1560 cm⁻¹ act as markers for the evolution of sp² hybridization within the carbon framework. The peak observed at 1330 cm⁻¹, known as the D band (I_D), is attributed to the A₁g mode of blowing in a ring and indicates the presence of structural flaws and irregularities within the material. On the other hand, the peak observed at around 1560 cm⁻¹, referred to as the G band (I_G), is linked to the E₂g vibrational mode, which is related to the sp² vibrational mode exhibiting two degenerate forms (Cheng et al., 2020; Deng et al., 2020).

According to Tuinstra and Koenig's law, the proportion of I_D/I_G indicates the degree of graphitization in graphitic carbons. A lower I_D/I_G ratio indicates improved graphitization (De *et al.*, 2020). Figure 3b presents the I_D/I_G ratios from all ACs for



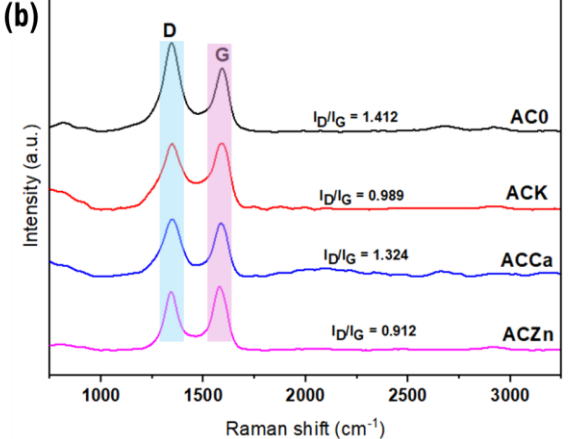


Fig. 3. (a) X-ray diffraction (XRD) characteristics of the activated carbon materials and (b) the Raman spectral profile of the product.

comparison analysis. The degree of graphitization for activated carbons obtained with various activating agents differs.

The KOH, CaCl₂, and ZnCl₂ self-activation methods enhance porosity in the activated carbon structure and increase the material's disorder. Incorporating an activating agent in producing biomass-derived-activated carbon enhances the impact of faults. The D peak's intensity escalates with an increase of faults, whilst the G peak's intensity diminishes, lowering the degree of graphitization (Nanda & Badhulika, 2022). Nonetheless, ACZn demonstrates the greatest extent of graphitization among RSS-derived activated carbons. Using CaCl₂ and ZnCl₂ enhances both porosity and graphitization in rubber seed shells. This atypical behavior will be further examined in the future.

The porosity of the activated carbon specimens was investigated through the physical adsorption of nitrogen. Porosity can generally be sorted according to the size and accessibility of their pores, with open pores being distinguished from closed ones. Figure 4 displays each activated carbon's equilibrium values for adsorpting and adding nitrogen. Each sample demonstrated a type-IV isotherm, as categorized by IUPAC, characterized by a pronounced hysteresis loop within the pressure span of 0.11–0.98 P/P₀, indicative of a mesoporous structure (Mei *et al.*, 2018). Notably, the quantity of nitrogen adsorbed at a P/P₀ value of 0.97 showed a marked higher,

Table 1. Porosity properties of RSS-based-porous carbon synthesized using various activating agents.

S_{BET} (m ² g ⁻¹)	D_{ap} (m ² g ⁻¹)	V_{tt} (cm 3 g $^{-1}$)
367.0	2.8	0.5
735.2	1.6	0.8
418.0	2.3	0.3
641.5	1.7	0.6
	367.0 735.2 418.0	367.0 2.8 735.2 1.6 418.0 2.3

 D_{ap} : average pore diameter, V_{tt} : total pore volume

particularly in samples activated with KOH and ZnCl₂, suggesting the presence of significant voids and/or mesopores within the material.

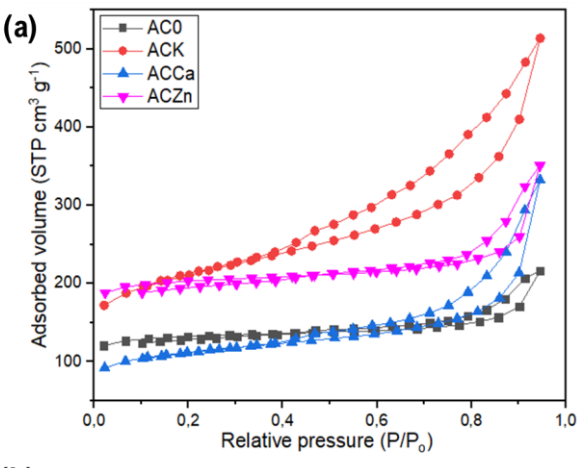
Figure 4a demonstrates a gradual reduction in the volume of nitrogen adsorbed with the addition of activating agents. The pore diameter profile analysis presented in Figure 4b corroborates the characteristics of the porous activated carbon, revealing specimens with pore sizes varying around 1.6 to 10 nm. Notably, some specimens illustrated in Figure 4b exhibited a pore diameter profile characterized by slim peaks within the 1.6 to 4.1 nm span, thereby under the significant impact of the activating agents on the pore architecture (Yadav *et al.*, 2021).

Table 1 delineates the Brunauer-Emmett-Teller surface area (S_{BET}) alongside the porosity properties of the activated carbon. According to Table 1, the RSS-derived activated carbon activated with KOH exhibits the largest surface area of 735.2 m² g⁻¹. After thermal treatment, $ZnCl_2$ and $CaCl_2$ significantly dehydrate lignocellulosic components (Prakoso *et al.*, 2022). The precursor's dehydration decreases particle size; however, this reduction is partially mitigated as the reactant stays enclosed during thermal treatment, serving as a template for porosity formation.

The proposed mechanism for porosity formation by salt-activating agents ($ZnCl_2$ and $CaCl_2$) is attributed to the voids left by the activating agent during the in-cleaning process. This idea relies on the opposites of the volumes of $ZnCl_2$ or $CaCl_2$ with the resultant micropore and mesopore volumes from the synthesized activated carbons. Only micropores are being formed, with mesoporous volume according to the reactant volume, indicating the template behavior of the activating agent.

The diminutive dimensions of the activating chemical molecule or its hydrates may elucidate the uniform and minute size of the resultant micropores. At elevated concentrations of the activating agent, where the growth of mesoporosity is significant, a discrepancy arises between the volumes, with the pore volume being less than that of the activating agent. The nature of this phenomenon has been clarified by asserting the intense assault on the unaltered material by the activating substance (Ouyang *et al.*, 2019; Zhang *et al.*, 2019).

KOH does not function as a dehydrating agent for the precursor. The chemical activation process that uses hydroxides involves removing carbon atoms from the carbon matrix and transforming them into inorganic compounds, such as carbonates. Simultaneously, a secondary mechanism unfolds in which metal atoms, produced through hydroxide reduction, are thought to intercalate between the graphene layers of the residual carbon, potentially enhancing the overall activation process (Hamza *et al.*, 2022). The activating agents initiate this reaction at temperatures surpassing 700 °C, and the hydroxide activation, as previously established, is characterized as a solid-liquid reaction, which is believed to progress according to the stoichiometric Equation (Kanjana *et al.*, 2021):



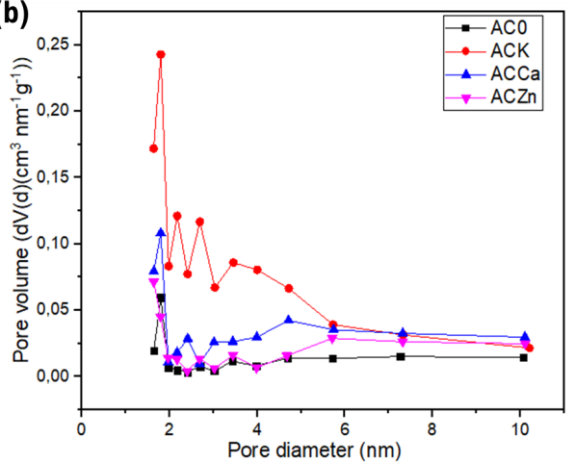


Fig. 4. The sample's distinctive (a) nitrogen adsorption-desorption isotherm and (b) pore size distribution profile.

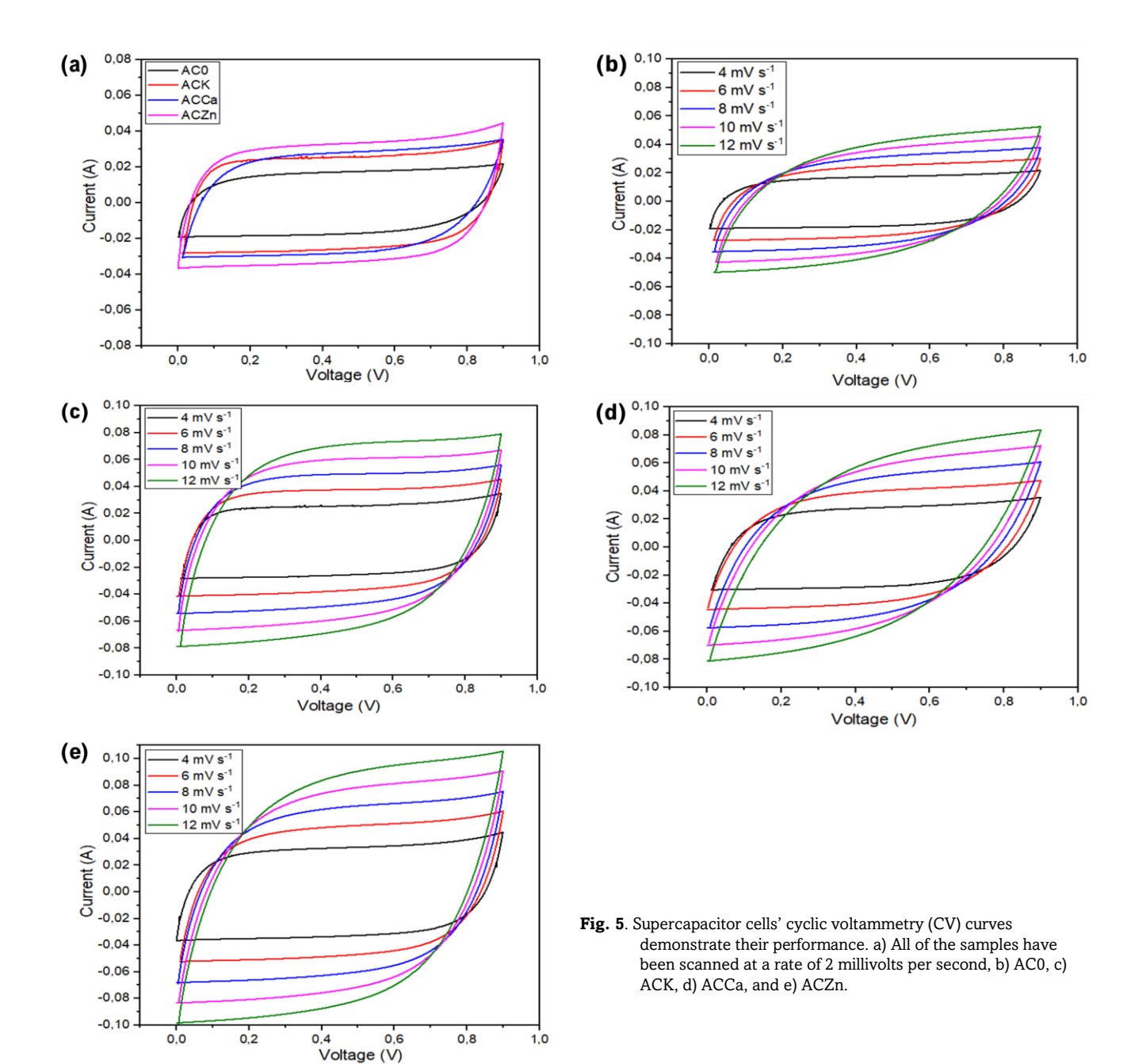
 $6 \text{ KOH} + 2C \rightarrow 2K + 3H_2 + 2K_2CO_3$

3.2. Electrochemical analysis

The electrochemistry behavior of all activated carbon was meticulously examined within a symmetrical electrode arrangement. CV characterization seeks to ascertain the supercapacitor's properties and capacitance worth. Figure 5a illustrates the cyclic voltammetry analysis of supercapacitors constructed from activated carbon generated from RSS, both with and without the activating agent, at a pace of scanning of 4 mV s⁻¹.

The voltammogram for ACZn-based supercapacitor cell approximates a quasi-rectangular shape devoid of redox phenomena. In their study, Wang *et al.* (2019) found that the ideal rectangular shape of the cyclic voltammogram is an indication of electric double-layer capacitance in which the adsorption of several ions on the surface of the electrode is the rate-determining step and is controlled by the diffusion rate of the electrolyte. As a further point of interest, the sample curves for ACK and ACCa are almost rectangular.

In their paper, Wolff *et al.* (2018) pointed out that the shape of the AC0 sample is a slanted trapezium, which indicates high rate capability, small IR drop, and high power. Since the ACZn material has the largest enclosed area among all the materials, it can be deduced that it has the highest capacitance. The cyclic voltammetry curve of AC0, ACK, ACCa, and ACZn



is presented at various scan rates (4–12 mV $\rm s^{-1}$), as shown in Figure 5b–e.

There is a positive correlation between increased scan rate and a clearer parallelogram shape formation in the cyclic voltammogram of all the samples that did not exhibit redox bursts. It is a signature of the absence of pseudocapacitive behavior, and therefore, the optimum performance is achieved (Mei et al., 2020). Capacitive features are suitable for the cyclic voltammogram when the scan rate is decreased. However, these ideal qualities are accompanied by disadvantages, such as increasing the scan rate and decreasing the capacitive behavior and features. This common phenomenon in activated carbon electrodes is ascribed to the restricted transport of ions and sorption in the narrow pores of large-grain materials at high scan rates. This leads to decreased specific capacitance (Zhou et al., 2023).

The capacitance drop is ascribed to the barriers for ion transfer out of the solution to the electrode superficies, which block mainly the electrode pores at higher scan rates (Wang *et al.*, 2019). The high specific surface area and the high extent of mesoporous structure enhance the ion adsorption into the active sites. The impact of the variation of the scan rate (4–12 mV s $^{-1}$) on the CV curve shape is also different for each sample

and is shown in Figure 5b-e.

The Galvanostatic charge-discharge curve, or the GCD curve, is a tool that gives an idea of the potential of the supercapacitor cells tested under constant current conditions. The potential was measured during charge and discharge, and GCD studies were performed at 30, 50, 70, and 100 milliamperes applied currents. The curves of the specimens in Figure 6 have a low voltage drop and symmetrical triangular shape, as suggested by Liu *et al.* (2016). These are characteristics of carbon-based supercapacitor cells.

0.0

100 150 200 250 300 350 400 450

Time (s)

Table 2. Capacitance, energy, and power density of supercapacitor at 25 mA $\rm g^{-1}$.

8 .				
Sample	C _{cell} (F g ⁻¹)	C _{sp} (F g ⁻¹)	E _{cell} (Wh kg ⁻¹)	P _{cell} (W kg ⁻¹)
AC0	35.6	142.5	3.2	134.1
ACK	53.7	215.0	4.8	191.1
ACCa	47.5	190.0	3.7	157.2
ACZn	61.5	246.0	5.5	246.0

Previous research has also demonstrated that a low potential is a good predictor of the good power characteristics of the supercapacitor cell (Hasegawa *et al.*, 2015). According to Bokhari *et al.*'s research from 2020, the GCD curve is used to establish the charging voltage compatible with the supercapacitor cells. According to Figure 6, the optimal potential for a single supercapacitor cell is observed to be

between 0.9 and 1.0 volts, which is the normal operating voltage of the cell.

Simulating the performance of the supercapacitor, Eqs. (3) and (4) were used; the findings are displayed in Table 2. The energy density was a minimum of 3.2 Wh kg⁻¹ for AC0 and a maximum of 5.5 Wh kg⁻¹ for ACZn. In addition, the power density was also the highest for ACZn with 246 W kg⁻¹, and the lowest for AC0 with 134 W kg⁻¹. Hence, the specific capacitance of the ACZn-based activated carbon was counted to be 267 F g⁻¹. These findings indicate that incorporating an activating agent in the synthesis of activated carbon greatly improves energy density and power output, scribed to the increased surface area and enhanced electrical conductivity of the activated carbon (Lemartinel *et al.*, 2022).

A high degree of graphitization guarantees superior conductivity in electrode materials. Nevertheless, the augmentation of sp² interaction between different types of

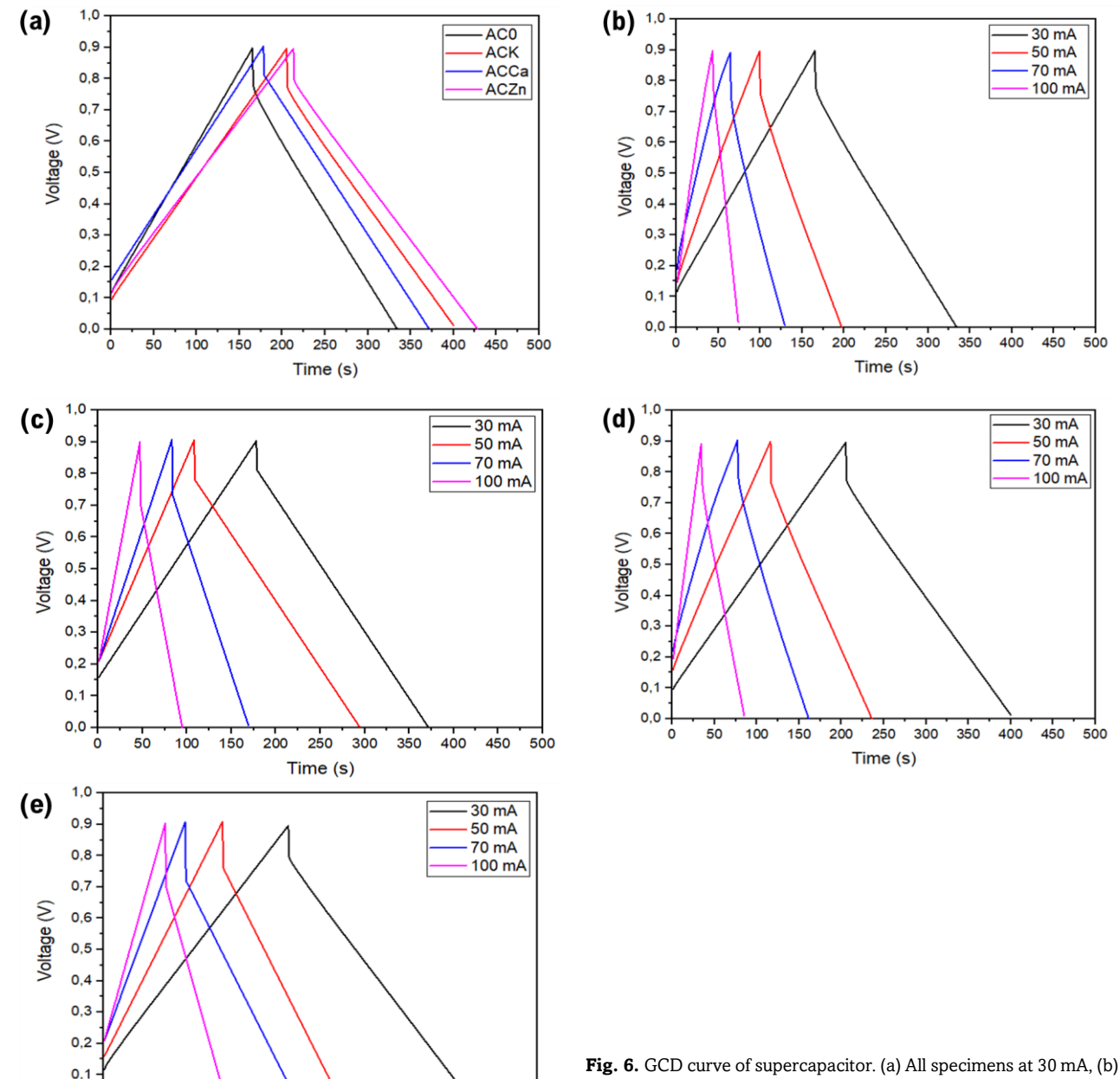


Fig. 6. GCD curve of supercapacitor. (a) All specimens at 30 mA, (b ACO, (c) ACK, (d) ACCa, and (e) ACZn.

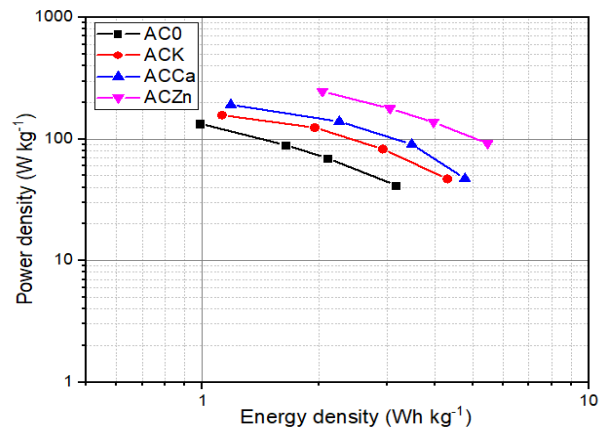


Fig. 7. Ragon plot supercapacitor cell based on all activated carbon.

carbon may inadvertently result in detrimental porosity, diminishing its ability to store charges and its particular surface area (Zhang *et al.*, 2022). Therefore, the material's charge transport and storage properties must be in a substantial state of balance. The rationale effectively elucidates the greatest $C_{\rm sp}$ value (246 F g⁻¹) attributed to ACZn, which possesses a greater degree of graphitization (low $I_{\rm D}/I_{\rm G}$ ratio) and a significantly lower surface area than ACK. The exceptionally small pore size distribution contributes to the elevated $C_{\rm sp}$ value of ACZn.

Figure 7 illustrates the Ragone plot, showcasing the cell's energy and power densities. According to this research, activated carbon with a mesoporous framework and an ordered pore architecture holds significant potential for enhancing energy density, owing to the synergistic effects of tailored pore distribution and improved electrochemical performance.

An extensive endurance evaluation of the ACZn electrode was performed, encompassing 5000 charge-discharge cycles within a voltage window of 0–0.9 V at a specific current 80 mA g $^{-1}$. The corresponding outcome is depicted in Fig. 8. Notably, the capacitance (C $_{\rm sp}$) exhibited an initial increment of approximately 0.11% over the first 1000 cycles, achieving a capacitance retention of 100.11%. By the 1000th cycle, the C $_{\rm sp}$ values stabilized at 100%, and this retention level was remarkably high for the remaining 5000 cycles. These findings highlight the exceptional electrochemical stability of the electrode.

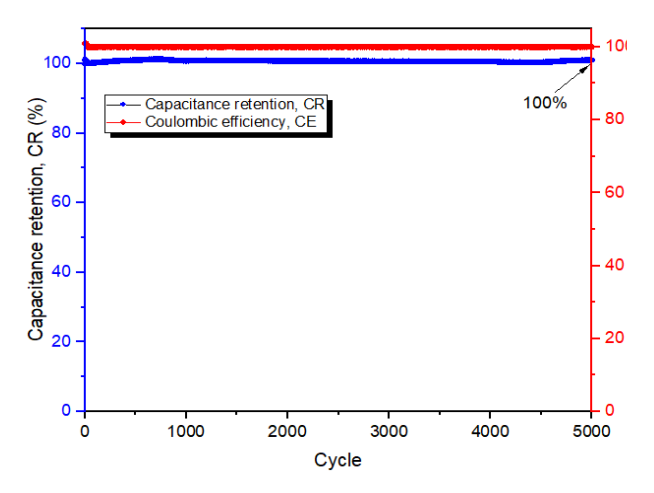


Fig. 8. The cyclic durability of the ACZn-based electrode supercapacitor.

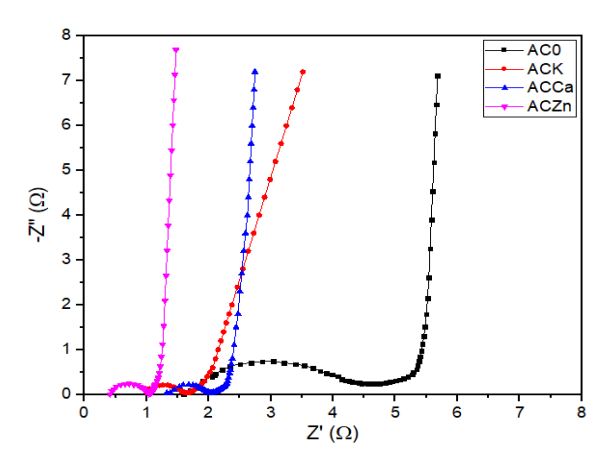


Fig. 9. The Nyquist plot illustrates the electrochemical impedance characteristics of all evaluated samples.

EIS, which stands for electrochemical impedance spectroscopy, was utilized to explore the interfacial dynamics at the interface between the electrolyte and the electrode (Vicentini $et\ al.$, 2021). Figure 9 gives the EIS data of the electrodes AC0, ACK, ACCa, and ACZn. This is something that can be observed at a glance. Based on the data that was collected, it was found that the electrolyte resistance (Rs) of AC0, ACK, ACCa, and ACZn were, respectively, 1.6, 1.0, 1.3, and 1.4 ohms. According to the findings, the values of the semicircular charge transfer resistance (Rct) were 4.0, 0.5, 0.6, and 0.4 ohms, and the Warburg impedance (Rw) values were 0.6, 0.6, 1.0, and 0.7 ohms, respectively.

The differences in electrolyte resistance at the electrode are influenced by the type of activation agent used, whereas the charge transfer resistance is fairly consistent among all the activated carbon materials; however, this value is quite variable for the unactivated activated carbon (Mei et al., 2018). From the findings, it is clear that the electrochemical properties of supercapacitor electrodes based on activated carbon electrodes, especially the specific capacitance (C_{sp}), are better for activators of potassium hydroxide, calcium chloride, and zinc chloride. This work indicates that it is possible to prepare activated carbon from biomass on an industrial scale. It suggests that employing reduced amounts of activators is a more environmentally friendly and sustainable way of activating carbon than the current methods (Kwiatkowski & Hu, 2021). Expanding on the proof of concept presented in this paper through application to real systems, this research, which builds on both physical and chemical activation approaches, will demonstrate the effectiveness of the suggested approach by comparing C_{sp} values with those from previous literature.

As shown in Table 3, the specific capacitance (C_{sp}) values of AC electrodes for supercapacitors generated from biomass can be compared. The results show that the C_{sp} values obtained from this work using hydrothermal and pyrolysis procedures are relatively high, as seen with the carbon values reported for other biomass sources in previously published works. This shows that developing more environmentally friendly synthesis methods for generating excellent supercapacitor electrodes from renewable materials is feasible.

4. Conclusion

The primary goal of this study was to find an ecologically friendly way to synthesize carbon-based compounds from rubber seed shells for use as supercapacitors. The

Table 3Capacitance values of activated carbon electrodes made from different biomass sources.

Source materials	Electrolyte	$C_{\rm sp}$ (F g ⁻¹)	Reference	
Wheat straw	3 М КОН	204	(Du et al., 2019)	_
Corn silk	6 M KOH	160	(Mitravinda et al., 2018)	
Biomass Straw	3 М КОН	250	(Guan et al., 2020)	
Cotton Stalk	1 M H_2SO_4	254	(Tian <i>et al.</i> , 2017)	
Soybean root	$EMIMBF_4$	216	(Guo et al., 2020)	
Bamboo	1 M Na ₂ SO ₄	120	(Chen et al., 2018)	
Peanut shell	1 M H_2SO_4	247.2	(Guo et al., 2019)	
Durian shell	1 M KOH	178	(Kanjana <i>et al.</i> , 2021)	
Oil palm empty fruits bunch	6 M KOH	176	(Rustamaji <i>et al.</i> , 2022)	
Rubber seed-shell	6 M KOH	246	Present work	

electrochemical properties of the porous carbon were determined by the porous framework, surface area, crystallinity, and degree of graphitization, all of which were significantly affected by the employment of different activating agents. The pore framework featured expansive mesopores with a narrow pore size distribution. At the same time, the crystallinity of the activat ed carbons exhibited well-defined planes, indicating short-range ordering within the graphitic layers. The engineered carbon electrodes demonstrated excellent electrochemical performance. The capacitance of the RSS-derived electrodes was largely dictated by the surface area, with the ZnCl2activated carbon achieving the highest capacitance of 246 F g due to its finely-tuned pore size distribution and balanced charge storage and transfer capabilities. Among the samples, the ACZn electrode emerged as the most promising for supercapacitor applications, offering superior capacitance, minimal polarization resistance, and exceptional reliability over 5000 cycles of storing and releasing. This work presents a sustainable pathway for producing activated carbon electrodes, contributing to the global circular economy and demonstrating considerable industrial potential.

Acknowledgments

The author would like to thank the University of Lampung for supporting this research through DIPA BLU 2024, the Chemical Engineering Instrumentation Laboratory of the University of Lampung, and the Process Safety and Electrochemical Energetic Laboratory, ITB.

Author Contributions: HR: creating content, analysis and revising, initial version, technique, collecting data, and conceptualized. TP: analysis, revising, monitoring, and examination. HD: revising, monitoring. PM: review & editing; PF: review & editing; SG: review & editing; DD: review & editing

Funding: The author(s) received no financial support for this article's research, authorship, and/or publication.

Reference

- Abdel Maksoud, M. I. A., Fahim, R. A., Shalan, A. E., Abd Elkodous, M., Olojede, S. O., Osman, A. I., Farrell, C., Al-Muhtaseb, A. H., Awed, A. S., Ashour, A. H., & Rooney, D. W. (2021). Advanced materials and technologies for supercapacitors used in energy conversion and storage: a review. *Environmental Chemistry Letters* 19(1), 375–439). https://doi.org/10.1007/s10311-020-01075-w
- Abdul, A. H., Ramli, N., Nordin, A. N., & Abd. Wahab, M. F. (2021). Supercapacitor performance with activated carbon and graphene nanoplatelets composite electrodes, and insights from

- the equivalent circuit model. *Carbon Trends*, 5. https://doi.org/10.1016/j.cartre.2021.100101
- Chen, W., Li, K., Xia, M., Chen, Y., Yang, H., Chen, Z., Chen, X., & Chen, H. (2018). Influence of NH3 concentration on biomass nitrogenenriched pyrolysis. *Bioresource Technology*, *263*, 350–357. https://doi.org/10.1016/j.biortech.2018.05.025
- Cheng, F., Yang, X., Dai, S., Song, D., Zhang, S., & Lu, W. (2020). Interweaving Activated Carbon with Multi-dimensional Carbon Nanomaterials for High-performance Supercapacitors. *Journal of The Electrochemical Society*, 167(4), 040507. https://doi.org/10.1149/1945-7111/ab71e4
- Cheng, F., Yang, X., Zhang, S., & Lu, W. (2020). Boosting the supercapacitor performances of activated carbon with carbon nanomaterials. *Journal of Power Sources*, 450. https://doi.org/10.1016/j.jpowsour.2019.227678
- Das, T., & Verma, B. (2019). High performance ternary polyaniline-acetylene black-cobalt ferrite hybrid system for supercapacitor electrodes. Synthetic Metals, 251, 65–74. https://doi.org/10.1016/j.synthmet.2019.03.025
- De, S., Acharya, S., Sahoo, S., & Chandra Nayak, G. (2020). Present status of biomass-derived carbon-based composites for supercapacitor application. In *Nanostructured, Functional, and Flexible Materials for Energy Conversion and Storage Systems* (pp. 373–415). https://doi.org/10.1016/B978-0-12-819552-9.00012-9
- Deng, H., Zhu, M., Jin, T., Cheng, C., Zheng, J., & Qian, Y. (2020). One-step synthesis of nitrogen, sulphur-codoped graphene as electrode material for supercapacitor with excellent cycling stability. *International Journal of Electrochemical Science*, 15(1), 16–25. https://doi.org/10.20964/2020.01.13
- Du, W., Zhang, Z., Du, L., Fan, X., Shen, Z., Ren, X., Zhao, Y., Wei, C., & Wei, S. (2019). Designing synthesis of porous biomass carbon from wheat straw and the functionalizing application in flexible, all-solid-state supercapacitors. *Journal of Alloys and Compounds*, 797, 1031–1040. https://doi.org/10.1016/j.jallcom.2019.05.207
- Dujearic-Stephane, K., Gupta, M., Kumar, A., Sharma, V., Pandit, S., Bocchetta, P., & Kumar, Y. (2021). The effect of modifications of activated carbon materials on the capacitive performance: surface, microstructure, and wettability. *Journal of Composites Science*, 5(3).. https://doi.org/10.3390/jcs5030066
- Gopalakrishnan, A., & Badhulika, S. (2020). Effect of self-doped heteroatoms on the performance of biomass-derived carbon for supercapacitor applications. *Journal of Power Sources*, 480. https://doi.org/10.1016/j.jpowsour.2020.228830
- Guan, M., Zhang, X., Wu, Y., Sun, Q., Dong, D., Zhang, X., & Wang, J. (2020). Biomass Straw Based Activated Porous Carbon Materials for High-Performance Supercapacitors. *Research and Application of Materials Science*, 1(2). https://doi.org/10.33142/msra.v1i2.1665
- Gunasekaran, S. S., Gopalakrishnan, A., Subashchandrabose, R., & Badhulika, S. (2021). Single Step, Direct Pyrolysis Assisted Synthesis of Nitrogen-Doped Porous Carbon Nanosheets Derived from Bamboo wood for High Energy Density Asymmetric Supercapacitor. *Journal of Energy Storage*, 42. https://doi.org/10.1016/j.est.2021.103048

- Guo, F., Jiang, X., Jia, X., Liang, S., Qian, L., & Rao, Z. (2019). Synthesis of biomass carbon electrode materials by bimetallic activation for the application in supercapacitors. *Journal of Electroanalytical Chemistry*, 844, 105–115. https://doi.org/10.1016/j.jelechem.2019.05.004
- Guo, N., Luo, W., Guo, R., Qiu, D., Zhao, Z., Wang, L., Jia, D., & Guo, J. (2020). Interconnected and hierarchical porous carbon derived from soybean root for ultrahigh rate supercapacitors. *Journal of Alloys and Compounds*, 834. https://doi.org/10.1016/j.jallcom.2020.155115
- Hamza, M., Li, J., Zhang, W., Zuo, Z., Liao, R., & Mei, B. A. (2022). Multi-scale electrochemical thermal model of Electric Double Layer Capacitor under galvanostatic cycling. *Journal of Power Sources*, 548. https://doi.org/10.1016/j.jpowsour.2022.231983
- Han, W., Wang, H., Xia, K., Chen, S., Yan, P., Deng, T., & Zhu, W. (2020). Superior nitrogen-doped activated carbon materials for water cleaning and energy storing prepared from renewable leather wastes. *Environment International*, 142. https://doi.org/10.1016/j.envint.2020.105846
- Hasegawa, G., Deguchi, T., Kanamori, K., Kobayashi, Y., Kageyama, H., Abe, T., & Nakanishi, K. (2015). High-Level Doping of Nitrogen, Phosphorus, and Sulfur into Activated Carbon Monoliths and Their Electrochemical Capacitances. *Chemistry of Materials*, 27(13), 4703–4712. https://doi.org/10.1021/acs.chemmater.5b01349
- Kanjana, K., Harding, P., Kwamman, T., Kingkam, W., & Chutimasakul, T. (2021). Biomass-derived activated carbons with extremely narrow pore size distribution via eco-friendly synthesis for supercapacitor application. *Biomass and Bioenergy*, 153. https://doi.org/10.1016/j.biombioe.2021.106206
- Kwiatkowski, M., & Hu, X. (2021). Analysis of the effect of conditions of preparation of nitrogen-doped activated carbons derived from lotus leaves by activation with sodium amide on the formation of their porous structure. *Materials*, 14(6). https://doi.org/10.3390/ma14061540
- Lawtae, P., & Tangsathitkulchai, C. (2021). The use of high surface area mesoporous-activated carbon from longan seed biomass for increasing capacity and kinetics of methylene blue adsorption from aqueous solution. *Molecules*, 26(21). https://doi.org/10.3390/molecules26216521
- Lemartinel, A., Castro, M., Fouché, O., De-Luca, J. C., & Feller, J. F. (2022). A Review of Nanocarbon-Based Solutions for the Structural Health Monitoring of Composite Parts Used in Renewable Energies. *Journal of Composites Science*,6(2). https://doi.org/10.3390/jcs6020032
- Lin, G., Liu, S., Qu, G., Song, Y., Li, T., Liu, F., & Hu, Y. (2021). Effect of pore size distribution in the gas diffusion layer adjusted by composite carbon black on fuel cell performance. *International Journal of Energy Research*, 45(5), 7689–7702. https://doi.org/10.1002/er.6350
- Liu, J., Deng, Y., Li, X., & Wang, L. (2016). Promising Nitrogen-Rich Porous Carbons Derived from One-Step Calcium Chloride Activation of Biomass-Based Waste for High Performance Supercapacitors. ACS Sustainable Chemistry and Engineering, 4(1), 177–187. https://doi.org/10.1021/acssuschemeng.5b00926
- Mei, B. A., Munteshari, O., Lau, J., Dunn, B., & Pilon, L. (2018). Physical Interpretations of Nyquist Plots for EDLC Electrodes and Devices. *Journal of Physical Chemistry C*, 122(1), 194–206. https://doi.org/10.1021/acs.jpcc.7b10582
- Mei, W., Duan, Q., Zhao, C., Lu, W., Sun, J., & Wang, Q. (2020). Three-dimensional layered electrochemical-thermal model for a lithium-ion pouch cell Part II. The effect of units number on the performance under adiabatic condition during the discharge. *International Journal of Heat and Mass Transfer*, 148. https://doi.org/10.1016/j.ijheatmasstransfer.2019.119082
- Mitravinda, T., Nanaji, K., Anandan, S., Jyothirmayi, A., Chakravadhanula, V. S. K., Sharma, C. S., & Rao, T. N. (2018). Facile Synthesis of Corn Silk Derived Nanoporous Carbon for an Improved Supercapacitor Performance. *Journal of The Electrochemical Society*, 165(14), A3369–A3379. https://doi.org/10.1149/2.0621814jes
- Mostazo-López, M. J., Salinas-Torres, D., Ruiz-Rosas, R., Morallón, E., & Cazorla-Amorós, D. (2019). Nitrogen-doped superporous

- activated carbons as electrocatalysts for the oxygen reduction reaction. *Materials*, 12(8). https://doi.org/10.3390/ma12081346
- Nanda, O. P., & Badhulika, S. (2022). Biomass derived Nitrogen, Sulphur, and Phosphorus self-doped micro-meso porous carbon for high-energy symmetric supercapacitor With a detailed study of the effect of different current collectors. *Journal of Energy Storage*, 56. https://doi.org/10.1016/j.est.2022.106042
- Ouyang, Z., Lei, Y., Chen, Y., Zhang, Z., Jiang, Z., Hu, J., & Lin, Y. (2019).

 Preparation and Specific Capacitance Properties of Sulfur,
 Nitrogen Co-Doped Graphene Quantum Dots. Nanoscale
 Research Letters, 14(1). https://doi.org/10.1186/s11671-019-3045-4
- Prakoso, T., Rustamaji, H., Yonathan, D., Devianto, H., Widiatmoko, P., Rizkiana, J., & Guan, G. (2022). The Study of Hydrothermal Carbonization and Activation Factors' Effect on Mesoporous Activated Carbon Production From Sargassum sp. Using a Multilevel Factorial Design. *Reaktor*, 22(2), 59–69. https://doi.org/10.14710/reaktor.22.2.59-69
- Rustamaji, H., Prakoso, T., Devianto, H., & Widiatmoko, P. (2023).

 Parameter study in preparation of nitrogen-rich-activated carbon for supercapacitors' application using multilevel factorial design.

 Materials Today: Proceedings. https://doi.org/10.1016/j.matpr.2023.04.163
- Rustamaji, H., Prakoso, T., Devianto, H., Widiatmoko, P., & Saputera, W. H. (2022). Urea nitrogenated mesoporous activated carbon derived from oil palm empty fruit bunch for high-performance supercapacitor. *Journal of Energy Storage*, 52. https://doi.org/10.1016/j.est.2022.104724
- Shabik, M. F., Begum, H., Rahman, M. M., Marwani, H. M., & Hasnat, M. A. (2020). Heterogeneous Kinetics of Thiourea Electro-Catalytic Oxidation Reactions on Palladium Surface in Aqueous Medium. Chemistry An Asian Journal, 15(24), 4327–4338. https://doi.org/10.1002/asia.202001016
- Simon, P., & Gogotsi, Y. (2020). Perspectives for electrochemical capacitors and related devices. *Nature Materials*, 19(11), 1151– 1163). https://doi.org/10.1038/s41563-020-0747-z
- Tagaya, T., Hatakeyama, Y., Shiraishi, S., Tsukada, H., Mostazo-López,
 M. J., Morallón, E., & Cazorla-Amorós, D. (2020). Nitrogen-Doped Seamless Activated Carbon Electrode with Excellent Durability for Electric Double Layer Capacitor. *Journal of The Electrochemical Society*, 167(6), 060523. https://doi.org/10.1149/1945-7111/ab8403
- Tian, X., Ma, H., Li, Z., Yan, S., Ma, L., Yu, F., Wang, G., Guo, X., Ma, Y., & Wong, C. (2017). Flute type micropores activated carbon from cotton stalk for high performance supercapacitors. *Journal of Power Sources*, 359, 88–96. https://doi.org/10.1016/j.jpowsour.2017.05.054
- Veeman, D., Shree, M. V., Sureshkumar, P., Jagadeesha, T., Natrayan, L., Ravichandran, M., & Paramasivam, P. (2021). Sustainable Development of Carbon Nanocomposites: Synthesis and Classification for Environmental Remediation. *Journal of Nanomaterials*, 2021. https://doi.org/10.1155/2021/5840645
- Vicentini, R., Aguiar, J. P., Beraldo, R., Venâncio, R., Rufino, F., Da Silva, L. M., & Zanin, H. (2021). Ragone Plots for Electrochemical Double-Layer Capacitors. *Batteries and Supercaps*, 4(8), 1291– 1303. https://doi.org/10.1002/batt.202100093
- Wang, C., Wang, H., Dang, B., Wang, Z., Shen, X., Li, C., & Sun, Q. (2020). Ultrahigh yield of nitrogen doped porous carbon from biomass waste for supercapacitor. *Renewable Energy*, 156, 370–376. https://doi.org/10.1016/j.renene.2020.04.092
- Wang, Y., Zhang, C., Qiao, X., Mansour, A. N., & Zhou, X. (2019). Three-dimensional modeling of mediator-enhanced solid-state supercapacitors. *Journal of Power Sources*, 423, 18–25. https://doi.org/10.1016/j.jpowsour.2019.03.012
- Wolff, N., Röder, F., & Krewer, U. (2018). Model Based Assessment of Performance of Lithium-Ion Batteries Using Single Ion Conducting Electrolytes. *Electrochimica Acta*, 284, 639–646. https://doi.org/10.1016/j.electacta.2018.07.125
- Wu, X., Mu, F., & Zhao, H. (2020). Recent progress in the synthesis of graphene/CNT composites and the energy-related applications. In *Journal of Materials Science and Technology*, 55, 16–34. https://doi.org/10.1016/j.jmst.2019.05.063
- Yadav, N., Yadav, N., & Hashmi, S. A. (2021). High-Energy-Density Carbon Supercapacitors Incorporating a Plastic-Crystal-Based

- Nonaqueous Redox-Active Gel Polymer Electrolyte. *ACS Applied Energy Materials*, 4(7), 6635–6649. https://doi.org/10.1021/acsaem.1c00703
- Yu, J., Li, X., Cui, Z., Chen, D., Pang, X., Zhang, Q., Shao, F., Dong, H., Yu, L., & Dong, L. (2021). Tailoring in-situ N, O, P, S-doped soybean-derived porous carbon with ultrahigh capacitance in both acidic and alkaline media. *Renewable Energy*, 163, 375–385. https://doi.org/10.1016/j.renene.2020.08.066
- Zhang, J. Y., Wang, X. T., Ali, S., & Liu, F. G. (2019). Analyzing electrical performance and thermal coupling of supercapacitor assembled using phosphorus-doped porous carbon/graphene composite. *Electronics* (Switzerland), 8(2). https://doi.org/10.3390/electronics8020254
- Zhang, S., Wang, K., Chen, H., Liu, H., Yang, L., Chen, Y., & Li, H. (2022).

 ZIF-67 derived in-situ grown N–Co3S4-GN/CNT interlinked conductive networks for high-performance especially cycling stable supercapacitors. *Carbon*, 194, 10–22. https://doi.org/10.1016/j.carbon.2022.03.054
- Zhao, J., & Burke, A. F. (2021). Review on supercapacitors: Technologies and performance evaluation. In *Journal of Energy Chemistry*, 59, 276–291. https://doi.org/10.1016/j.jechem.2020.11.013
- Zhou, W., Liu, Z., Chen, W., Sun, X., Luo, M., Zhang, X., Li, C., An, Y., Song, S., Wang, K., & Zhang, X. (2023). A Review on Thermal Behaviors and Thermal Management Systems for Supercapacitors.

 Batteries, 9(2). https://doi.org/10.3390/batteries9020128



© 2025. The author (s). This article is an open-access article distributed under the terms and conditions of the Creative Commons Attribution-ShareAlike 4.0 (CC BY-SA) International License (http://creativecommons.org/licenses/by-sa/4.0/)